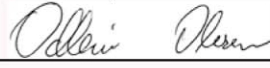


NGU Report 2009.017

The Mjølner Impact Structure in Time and Space

Report no.: 2009.017		ISSN 0800-3416	Grading: Open
Title: The Mjølner Impact Structure in Time and Space			
Authors: Stephanie C. Werner, Trond H. Torsvik		Client:	
County:		Commune:	
Map-sheet name (M=1:250.000)		Map-sheet no. and -name (M=1:50.000)	
Deposit name and grid-reference:		Number of pages: 27	Price (NOK): 135.-
Fieldwork carried out:		Date of report: 20.02.2009	Project no.: 3140.00
		Person responsible: 	
<p>Summary:</p> <p>The Mjølner impact crater was discovered in seismic reflection data in the 1990's and the detailed structure is well established. The submarine crater, situated in the southwestern Barents Sea, is believed to have a crater diameter of about 40 km, and a shallow relief (about 50 m). The crater is buried under a layer of sediments. Stratigraphic relationships (drill core 7329/03-U01) indicate a Cretaceous formation age at around 140 Ma. This structure is a well-studied crater, but still the dimensions and subsequent history need further investigation.</p> <p>Here, density and magnetic susceptibility measurements of core samples are presented and used to interpret a newly available aeromagnetic survey (BAS-06) and gravity data, and to forward model the potential field anomaly data of the area, in order to better constrain the signature of the crater. Preliminary modelling suggests that the crater diameter is overestimated. We have also developed a detailed Cretaceous palaeogeographic reconstruction at the time of impact. This investigation is conducted to support future drilling at the Mjølner impact site.</p>			
Keywords: Geofysikk		Gravimetri	Magnetometri
Tolkning			

CONTENTS

1. Introduction	6
2. Geological and palaeogeographical setting.....	6
2.1 The Geological Setting.....	6
2.2 Cretaceous palaeogeographic setting	7
2.3 The Barents Sea in time and space.....	7
3. Magnetic properties and densities of core 7329/03-U-01	9
4. Magnetic and Gravity Data	11
4.1 The Mjølfnir magnetic anomaly	11
4.2 The Mjølfnir Free Air Gravity Anomaly.....	14
5. The Structural Interpretation of Mjølfnir.....	16
6. Conclusions	20
7. Acknowledgements	21
8. References	22
9. Figures.....	24
10. Tables	25
11. Appendix	26
11.1 Susceptibility and Density Measurements:	26

1. INTRODUCTION

Gudlaugsson (1993) discovered the Mjøltnir impact crater in seismic reflection data, and the crater structure is now apparently well established. This submarine impact crater, located in the southwest Barents Sea, is estimated to have a crater diameter of about 40 km and a shallow relief of about 50 m. Nonetheless, the dimensions other than the relief remain undetermined. The crater is buried beneath a few hundred meters thick layer of sediments. Stratigraphic relationships (drill core 7329/03-U01; 1998; IKU Petroleum Research) suggest a Lower Cretaceous impact age at around 142 Ma (Dypvik et al., 2004). In this account, density and magnetic susceptibility measurements of core-samples from core 7329/03-U01 are presented and subsequently used to interpret a new aeromagnetic survey and existing gravity data, and to model the potential field data in an attempt to better constrain the signature of the crater. We also present an Early Cretaceous reconstruction at impact time and calculate the drift of the Barents Sea realm from the Late Palaeozoic (Carboniferous) to recent times.

2. GEOLOGICAL AND PALAEOGEOGRAPHICAL SETTING

2.1 The Geological Setting

The impact site ($73^{\circ}48' N$, $29^{\circ}40' E$) is located at the Bjarmeland platform (Fig. 1), a shallow shelf characterized by a relatively undisturbed and complete Carboniferous-Quaternary stratigraphic section. The underlying crystalline basement is assumed to be of Palaeozoic age and identified at depths in the order of 7 to 9 km (Johansen et al., 1993). Sedimentary strata are almost horizontal, even though two prominent seismic reflectors, Top Permian and Base Cretaceous, show a slight dip to the south (Breivik et al., 1995). The current water depth ranges between 350 to 400 meters whilst the

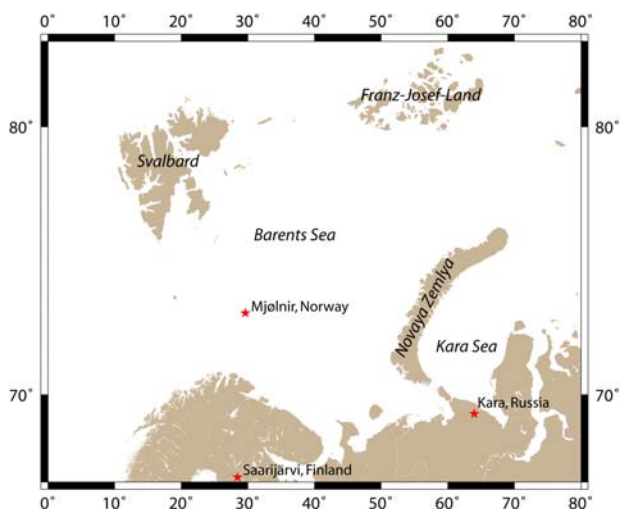
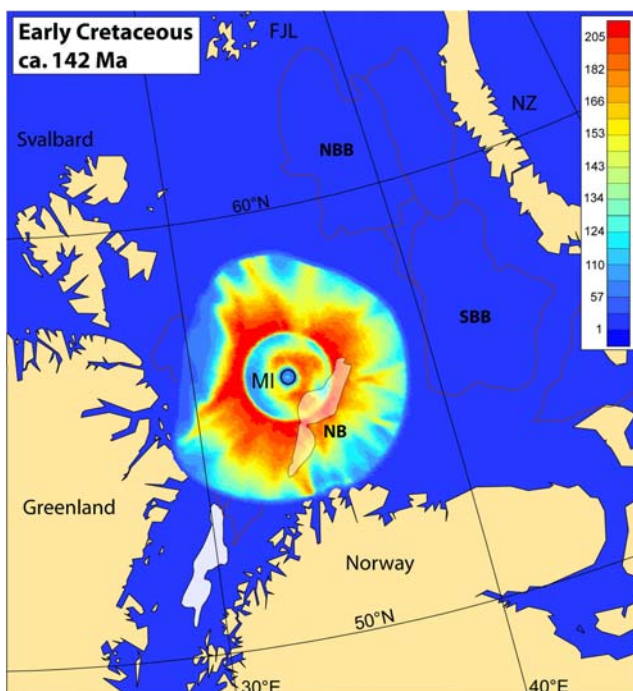


Fig. 1: The location of Mjøltnir impact site ($73^{\circ}48' N$, $29^{\circ}40' E$) within the southwestern Barents Sea.

palaeo-water depth at impact time was suggested to range between 350 and 500 meters (Gudlaugsson, 1993; Dypvik et al., 1996; Smelror et al., 2001; Tsikalas et al., 2002). The impact event affected the stratified sediments to a depth of about 4 km, recognized as disturbed strata in seismic profiles.

2.2 Cretaceous palaeogeographic setting

Indicators for the impact origin of the structure are found in drill cores 7430/10-U-01 and 7329/03-U-01 (1988, 1998 IKU Petroleum Research) and in equivalent layers exposed on Svalbard that are enriched in iridium and shocked quartz — both are found in the ejecta related layer. The age of the crater has been estimated from biostratigraphy and indicates that the impact event occurred at the Volgian-Ryazanian boundary (142 ± 6 Million years ago). A 142 million year plate reconstruction (Fig. 2) shows that the Barents Sea region was centred on the 60°N parallel. The impact palaeolatitude is calculated to 56.4°N , at a time when Greenland also bordered and defined the western margin of the Barents Sea. Thus, and with relevance to tsunami modelling of the impact, the distance to Greenland (ca. 300 km) was



approximately the same as to Northern Norway (Finnmark) where waves as high as 100 meters have been estimated (Glimsdal et al., 2007).

Fig. 2: The palaeogeographic setting of the Mjølnir impact site reconstructed to the Lower Cretaceous, ca.142 Ma. The main differences with respect to the current setting are the palaeo-latitude of 56.4°N and the then young and narrow Atlantic Ocean. The estimated tsunami wave height (after Glimsdal et al., 2007) and sedimentary basin outlines are draped on the reconstruction.

2.3 The Barents Sea in time and space

The Barents Sea realm has drifted northward over the past 300 Ma, crossing tropic and subtropic latitudes as confirmed in the sedimentary record (Fig. 3). Fauna and sedimentary facies

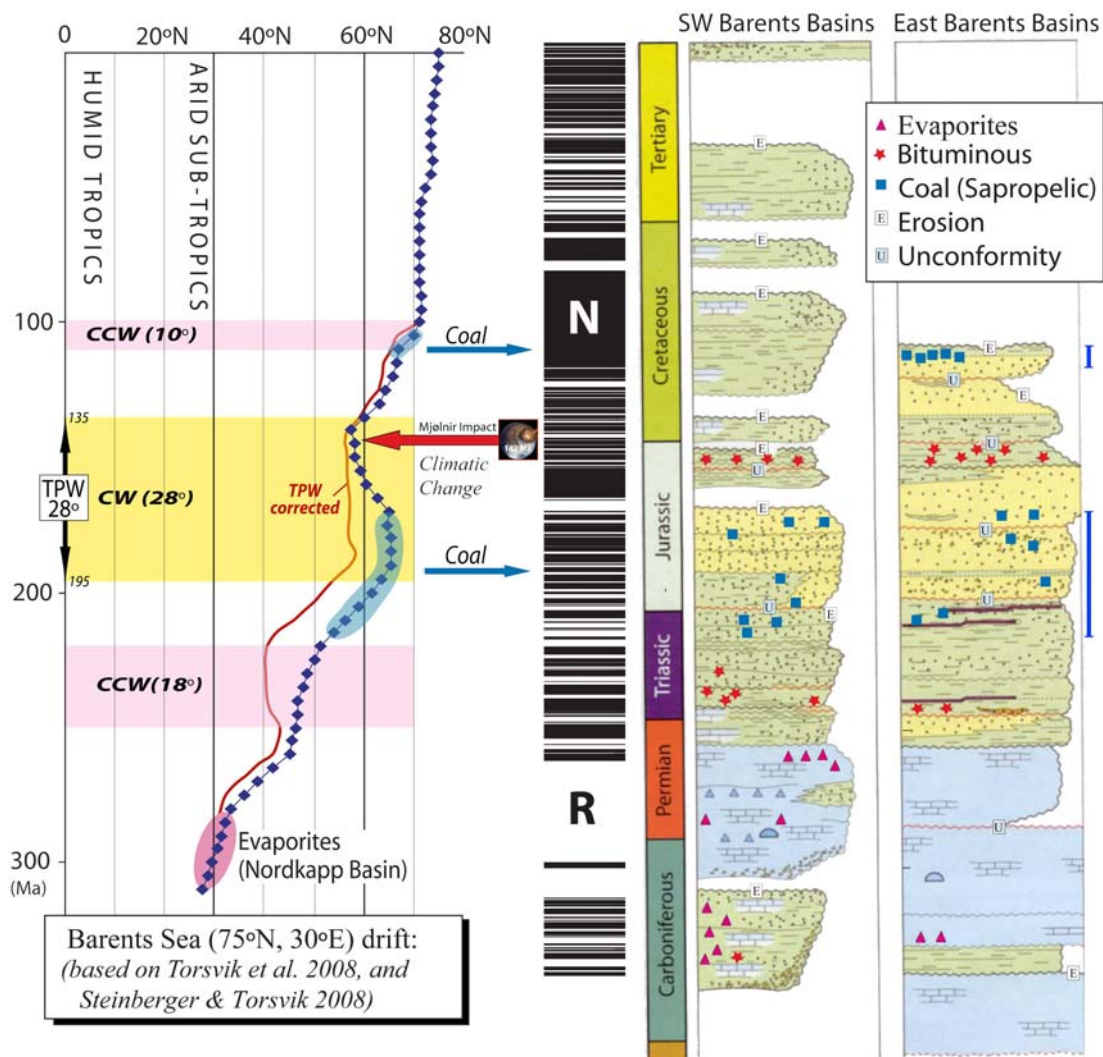


Fig. 3: The Barents Sea in space and time. Along with the stratigraphic column for the southwestern Barents Sea and the Western Barents Sea basins, the magnetic polarity, the latitudinal drift of the Mjølner impact site is shown. The drift curve is derived from a global apparent polar wander path with (red curve) and without (blue curve) corrections for true polar wander (TPW). The TPW corrected curve shows a general northward movement of the Barents Sea realm (with respect to the mantle) but the flat Jurassic-Early Cretaceous section of the curve show that the apparent Mid-Late Jurassic southward movement (with respect to the spin-axis) is an artefact of TPW.

are sensitive to climate changes and thus to latitude. Distribution of evaporites, coal and certain carbonates are strongly latitudinally dependent. Evaporites are mostly deposited in arid sub-tropical regions whilst coal is formed in wet equatorial regions or the northerly and southerly wet belts. This is well exemplified for the Barents Sea realm: 300 million years ago the Barents Sea was at sub-tropical latitudes, a palaeolatitude that fits well with the occurrences of Late Carboniferous-Early Permian evaporites in the Nordkapp Basin. Subsequently the Barents Sea drifted northward, and by Jurassic time, we find coal that witnesses that the region had entered the northern wet belt. We also show that the Barents Sea region drifted southward during Mid-Late Jurassic before continued northward drift (incidentally coinciding with the Mjølner impact event) with coal once again appearing in the

East Barents stratigraphy (Fig. 3). These back-and-forth N-S movements (ca. five degrees in total) led to a climatic change, not because of 'continental drift' but due to true polar wander (TPW). TPW is the rotation of the entire solid Earth's outer shell with respect to the spin-axis, and during Jurassic and Early Cretaceous time (195 to 135 Ma) the entire Earth rotated ca. 28° clockwise (Steinberger and Torsvik, 2008). This led to slow climatic changes with some areas becoming warmer, such as the Barents Sea moving away from the spin axis, whilst others became colder.

3. MAGNETIC PROPERTIES AND DENSITIES OF CORE 7329/03-U-01

The Mjølnir drill core confirmed the impact origin revealing disturbed sedimentary layers and an iridium-rich layer just above the disturbed sequence (Dypvik et al., 2004). Even though the drill core gives insight to rock properties and impact-related stratigraphic disturbance, the core never penetrated the uplifted deeper layers as observed in seismic sections reaching only a depth of 171 meters below the sea floor.

Here we present measurements of magnetic properties and densities for two sample sets. Susceptibilities were measured using a Bartington MS2c sensor in a core-scanning set-up. Sampling was limited by the physical condition of the core, as the instrument set-up requires intact core-sections of at least 10 cm in length. For this sample-set only total susceptibilities were measured (Fig. 4). The second dataset consists of selected samples investigated in a laboratory environment (Torsvik and Olesen, 1988), and both volume-specific susceptibilities and densities were determined (Fig. 4). Susceptibility values ranged between zero (i.e. below the instrument noise level) and 200×10^{-5} SI, common values for marine sedimentary rocks. The sample selection is biased to competent samples. Overall, maximum susceptibility values are found in samples with rusty colours. Typical magnetic sources in such a sedimentary environment aside the bedrock are deposited detrital magnetic minerals and siderite-cemented beds or nodules aside.

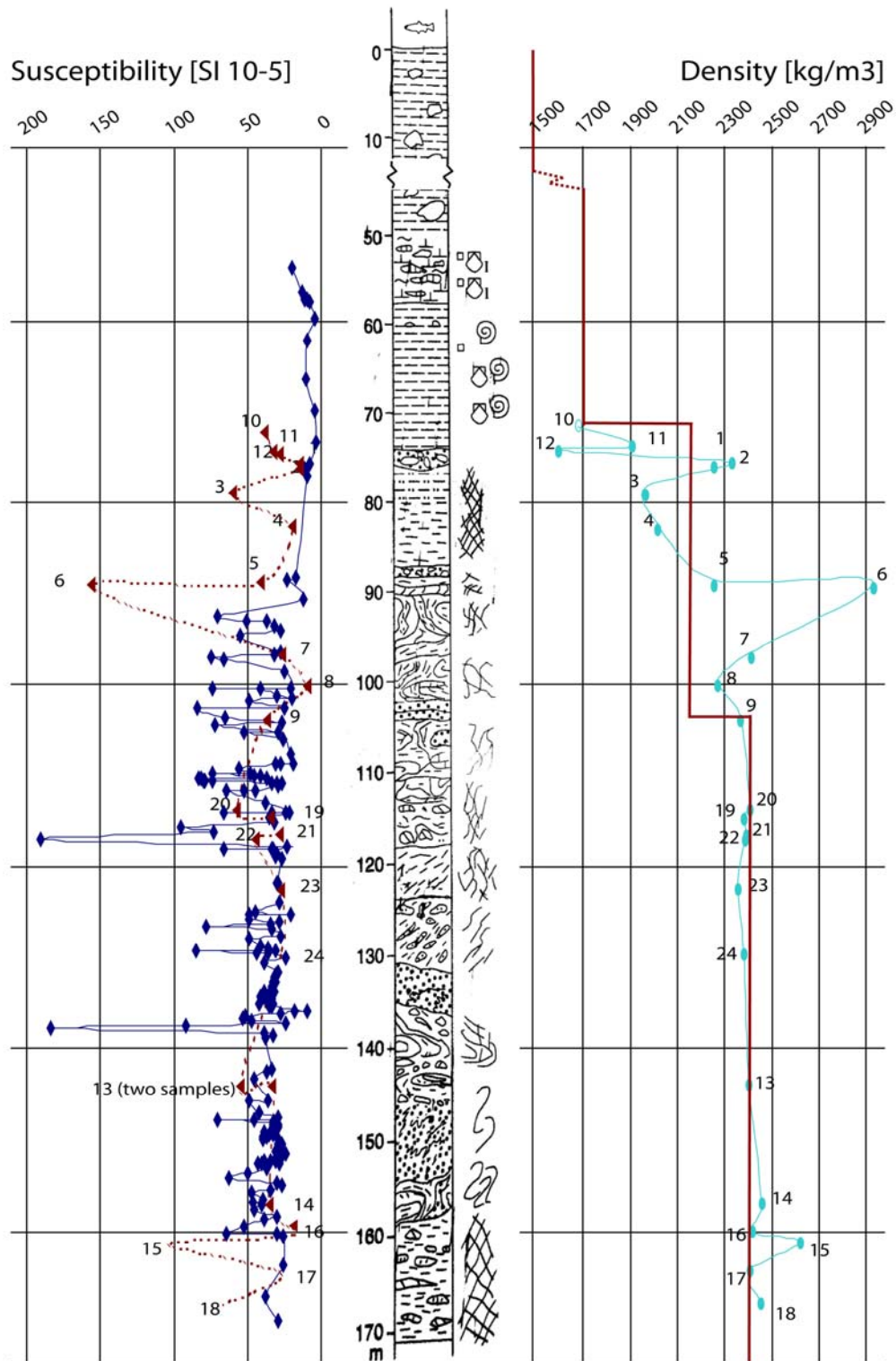


Fig. 4: The stratigraphy of core 7329/03-U-01 (Mørk, pers. comm. 2006) and measurements of susceptibilities (left) and densities (right) of competent samples. The red curve indicates the density variations with depth as used for the upper most layers of the density model.

The measured densities range between 1500 and 2900 kg/m³ and mostly around 2400 kg/m³ (Fig. 4). This selection is also biased to more competent core sections because of the density measuring procedure, i.e. "Archimedes" principle, that does not allow measurements of unconsolidated sediments. The densities determined here are dry densities, because any persistent exposure to water would have dissolved most samples. The two extreme end-members are related to materials such as coal (sample 12) or siderite nodules (sample 6). Generally, the densities increase with depth likely due to compaction. During the drilling, the first 60 meters were penetrated without recovering the core. These first layers are unconsolidated Quaternary sediments, which have densities less than 1700 and as low as 1300 kg/m³. Following the density measurements of the core samples, densities for the uppermost layers of the subsurface model of Mjølnir were derived and are plotted in Fig. 4.

4. MAGNETIC AND GRAVITY DATA

The southwest Barents Sea is explored by a number of seismic, gravity and magnetic surveys due to substantial exploration interest in this petroleum frontier area (Fig. 5a). Seismic data originally led to the discovery and definition of the shape of the subsurface structure of Mjølnir. Nevertheless, the seismic data only revealed the palaeo-relief of the impact structure and the volume influenced by the impact event. Prominent is the disturbance of the stratification of the sediments due to the impact event while circumjacent it is still well observable. No apparent or actual crater floor or melt sheet were identified. Additional information from gravity and magnetic data were gathered, but until now, no detailed modelling was undertaken.

4.1 The Mjølnir magnetic anomaly

Earlier (ship-borne) magnetic measurements were collected together with gravity and seismic measurements in three profiles crossing the structure diagonally. After processing (e.g. Tsikalas et al., 1998b), the remaining low-amplitude anomalies range between -75 nT and 20 nT, a magnetic anomaly (20 nT) was interpreted as central anomaly, which is slightly offset from the topographic centre. This relative high is surrounded by relative lows correlating to the outer crater zone, and the anomaly pattern looks like cloverleaves (Fig. 5b). Considering

the profile set up, the cloverleaf pattern, could be result of the interpolation of insufficiently diurnal-corrected profiles.

During 2006, a new data set was collected of which a small portion is presented here. This aeromagnetic survey (BAS-06, Gernigon et al., 2007) was flown in an in-line-tie-line configuration above the southwestern Norwegian Barents Sea area. The general N-S oriented lines have a spacing of 2 km with E-W oriented tie-lines of 6-km spacing. In the Mjølnir area, the lines were filled to 1 km line spacing (Fig. 5a, red track-lines). The sensor, a caesium magnetometer, recorded the magnetic field at an altitude of 230 m with an aeroplane groundspeed of 225 km/h; the resulting spatial sampling interval is 12-14 meters. Magnetic measurements, notably in the high arctic are often affected by diurnals. Base-station reference measurements at distances of 300 to 600 km away are not always reflecting local disturbances, and therefore such measurements are difficult to correct. During the survey, diurnals were recorded and roughly 10% of the profiles had to be re-flown due to high noise level. The data were treated by standard processing which included: filtering for noise created by the manoeuvring, statistical-levelling and micro-levelling using Geosoft OASIS montaj routines, and median-filtering (Mauring and Kihle, 2006) to correct for the diurnals. The data portion of the total magnetic field variations measured during the new aeromagnetic survey BAS-06 presented here covers the area of Mjølnir and surroundings and shows low-amplitude anomalies with a regional low close to the Mjølnir impact site (Fig. 5b). The amplitude range found in this region is ca. 150 nT, while the area related to Mjølnir only shows variations in the order of 25 nT. High-pass filtering with cut-off wavelengths of 10 km or 20 km was applied to extract the shallow sources in the study area. The patchy distribution of impact melt could result on a crustal magnetic anomaly map in higher frequency content than e.g. visible on gravity maps. On the other hand, a smoothing of magnetic anomalies around an impact site has been observed for structures in crystalline environment (e.g. Suvasvesi N, Finland; Pesonen et al., 1996). A possible correlation between a relative minimum in the magnetic field and the crater outline can be observed (Fig. 5c). The dataset suffers from a low signal-to-noise level. No short-wavelength anomalies related to the crater can clearly be separated when a high-pass filter is applied (Fig. 5d and 5e). The statistical uncertainties are at the level of 1-3 nT for the entire survey, and therefore wavelengths less than ten kilometres cannot be separated above the noise level (Fig. 5d). Using a cut-off wavelength of 20 km reliable anomalies can be separated (range about 6 nT), but they are unlikely to be induced by crater related structures.

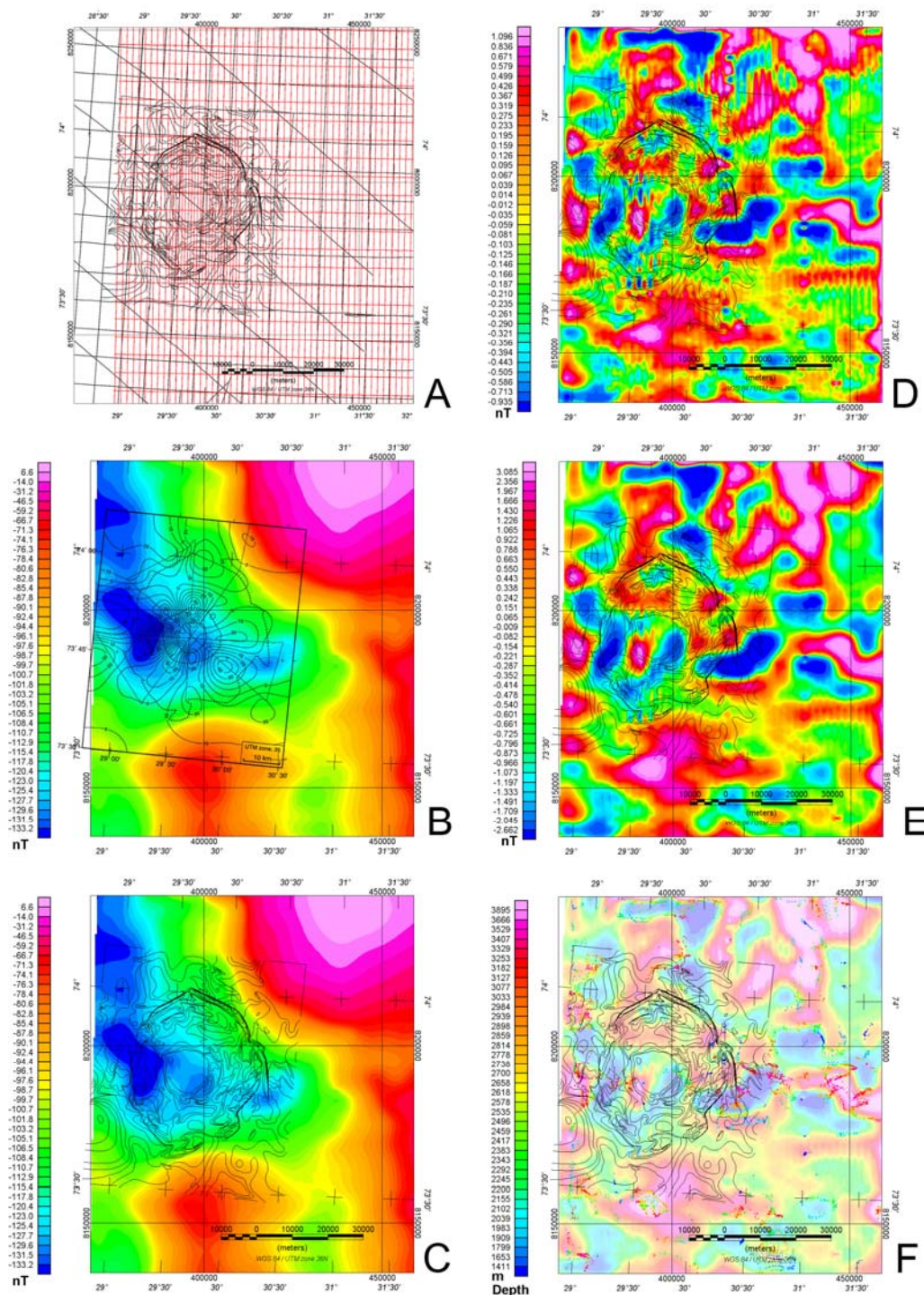


Fig. 5: The aeromagnetic anomaly map as surveyed during the BAS 06 campaign. (a) Aeromagnetic measurements were performed along flight lines shown in red. Ship recordings of gravity and seismics are shown as black track lines. (b) The aeromagnetic anomaly map in comparison with the anomaly map of Tsikalas et al. (1998b); (c) the same in comparison with the palaeo-relief of Mjøltnir as interpreted from seismic data by Tsikalas et al. (1998a,b,c); (d) palaeo-relief and a 10-km Gaussian high-pass filtered magnetic anomaly and (e) 20-km Gaussian high-pass filtered magnetic anomaly map; (f) example of the results of an Euler deconvolution with a structural index of $SI=1$ and a tolerance of 7 % applied to the 20-km Gaussian high-pass filtered magnetic anomaly in comparison with the palaeo-relief.

An example of Euler deconvolution is shown in comparison with the 20-km Gaussian high-pass filtered anomaly map (Fig. 5f). The structural index is that of sheet-like source distribution, such as expected for melt patches. Euler deconvolution applied to the gridded data only yielded depths outside the expected crater depth-diameter dimensions, independently of which structural index was chosen or if applied to filtered (low-pass) or unfiltered data. We applied Euler deconvolution (Reid et al., 1990) also to in-line profiles that have a much higher sampling rate and frequency content than the gridded data. The only layer, which was confidentially identified, is the seafloor! Considering the host material of the Bjarmeland Platform being largely non-magnetic, anomaly variations of only a few nT are expected. Mostly undisturbed horizontal strata characterize the Bjarmeland Platform, and no significant anomaly generated by the sediments is expected in this area around the impact structure. The sources contributing to the long-wavelength content of the observed crustal field are related to the bedrock horizon, situated much deeper than any volume influenced by the impact crater. From the susceptibility and density measurements and the core interpretation, only detrital magnetic minerals and siderite-cemented beds or nodules aside the bedrock can be considered as the source for magnetisation observed in this study area. Such a result - the macroscopic invisibility of the crater - is expected for sedimentary areas such as in the Barents Sea, unless the projectile “delivered” magnetic material.

None of the features found in the new data set (Fig. 5b) resemble the magnetic anomaly pattern of the interpolated shipborne data map by Tsikalas et al. (1998b). Actually, a few of the features are inverted, although this could be related to an artefact of overcompensation due to trend correction on the earlier data set.

4.2 The Mjølner Free Air Gravity Anomaly

The Barents Sea area is substantially covered by seismic lines and gravity profiles (Fig. 5a, black track-lines). The crater appears well preserved under layers of unconsolidated and consolidated sediments about 500 m thick, and overlain by a shallow water column (about 350 m). Tsikalas and others (in a series of papers in 1998, Tsikalas et al., 1998a, b, c) utilized seismic reflection lines and well data to derive detailed sub-post-impact sedimentary as well as the deeper structural extent (Fig. 6a).

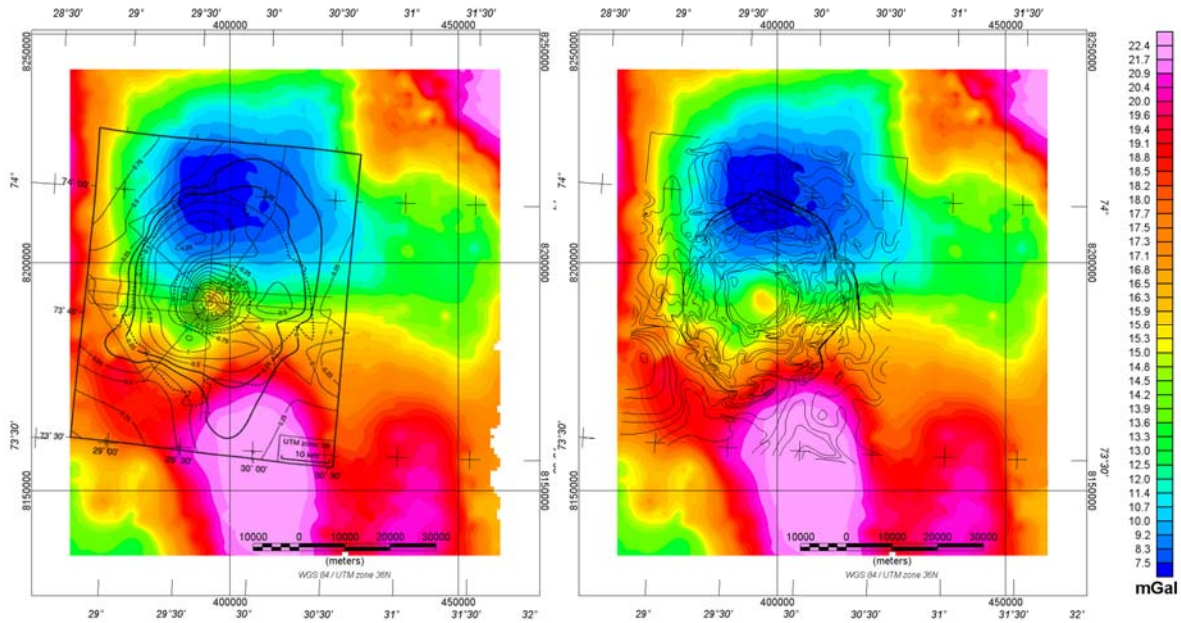


Fig. 6: Free air gravity anomaly map (Skilbrei et al., 2000) in comparison with the palaeo-relief of Mjøltnir (right), derived from seismic data by Tsikalas et al. (1998a, b, c), and (left) the gravity anomaly map provided by Tsikalas et al. (1998b).

The most prominent feature of the crater is the central uplift, which is well preserved under the sediments, and more or less the only feature recognizable in the gravity map. Tsikalas et al. (1998b,c) described the extent of uplift with a diameter of about 8 kilometers, surrounded by a trough of about 4 km in width and further a 12-km wide outer zone. We observe a relative gravity low of about 3-4 mGal coinciding with the extent of the “seismic disturbance” and a relative high (2 mGal) along with the uplifted structure observed in the seismic profiles. The full extent of the crater is unclear (Fig. 6b). Similarly, the anomaly was described by Tsikalas et al. (1998b), but a detailed comparison is impossible, because their data were filtered and trend-corrected. Subtraction of regional fields as well as band-pass filtering usually result in distortion of the residual anomaly and of the shape of the interpreted subsurface structure. Stripping methods, which use detailed geological information to calculate and subtract the known contributions from the observations (Hammer, 1963), lead to a better understanding of the residual anomaly. The data are presented here with and without further trend correction, but no filtering.

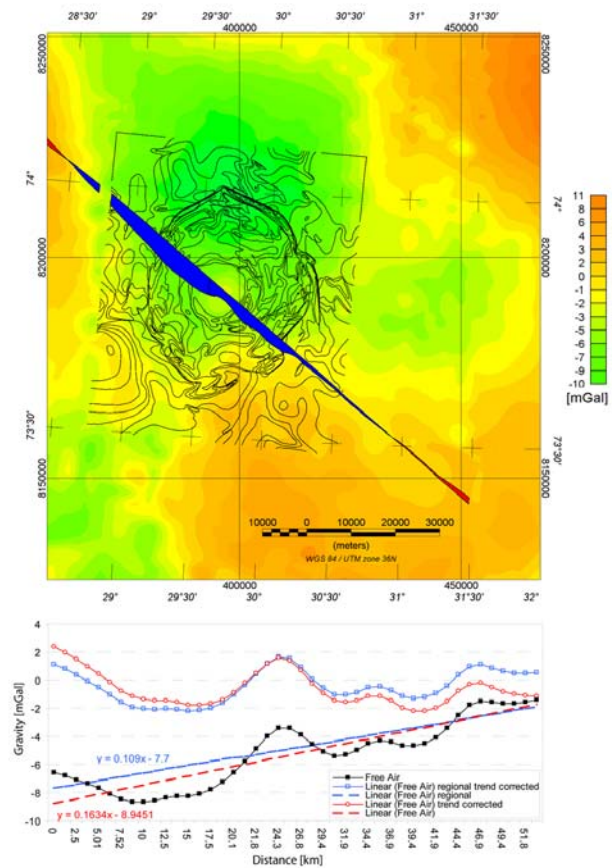
This results, as pointed out above, in a shift of the relative maximum of the gravity anomaly above the structural central peak and a slight distortion of the anomaly representing the crater. Such an offset due to data correction subsequently leads to an interpretation of an asymmetric shape. If considering a more regional view, no simple regional trend can be defined (Fig. 7a).

5. THE STRUCTURAL INTERPRETATION OF MJÖLNIR

We modelled the sub-surface structure using a forward 2D modelling method (originally developed by Talwani et al. (1959)). We decided to model along a profile in NW-SE orientation (Fig. 7a) that coincides with seismic sections based on high-resolution single-channel and multi-channel recordings (Tsikalas et al., 1998a,b,c; Gudlaugsson, 1993). From the aeromagnetic data, no signal can be clearly related to a source related to the impact structure, therefore we focused on the gravity data. For the gravity field modelling, simple structural assumptions have been made, making use of the densities derived from the core (Fig. 4), typical morphologies of a complex crater (Melosh, 1989), and relevant seismic lines (Tsikalas et al., 1998a,b,c; Gudlaugsson, 1993).

We used the gravity anomaly as observed, with and without correction for a regional linear trend. Fig. 7b shows the original and trend-corrected profile. Such linear trends often represent long wavelength contributions from the basement or even deeper anomaly sources. We modelled the impact crater for both uncorrected and trend-corrected anomaly residuals to further constrain the basement interface, which is not resolved in the available seismic sections.

Fig. 7: Free air gravity anomaly map (top) in comparison with the palaeo-relief including on of the gravity profile across the structure in NW –SE direction, which coincides with two seismic lines, used in the 2D gravity modelling, profile plot (bottom), derived linear trends, as well as the trend corrected version of the anomaly.



The resulting but preliminary model is shown in Fig. 8 for the trend corrected case, together with two seismic profiles along which we modelled. Typically for complex craters, two major characteristics contribute to the gravity anomaly: (1) the cavity including possibly reduced

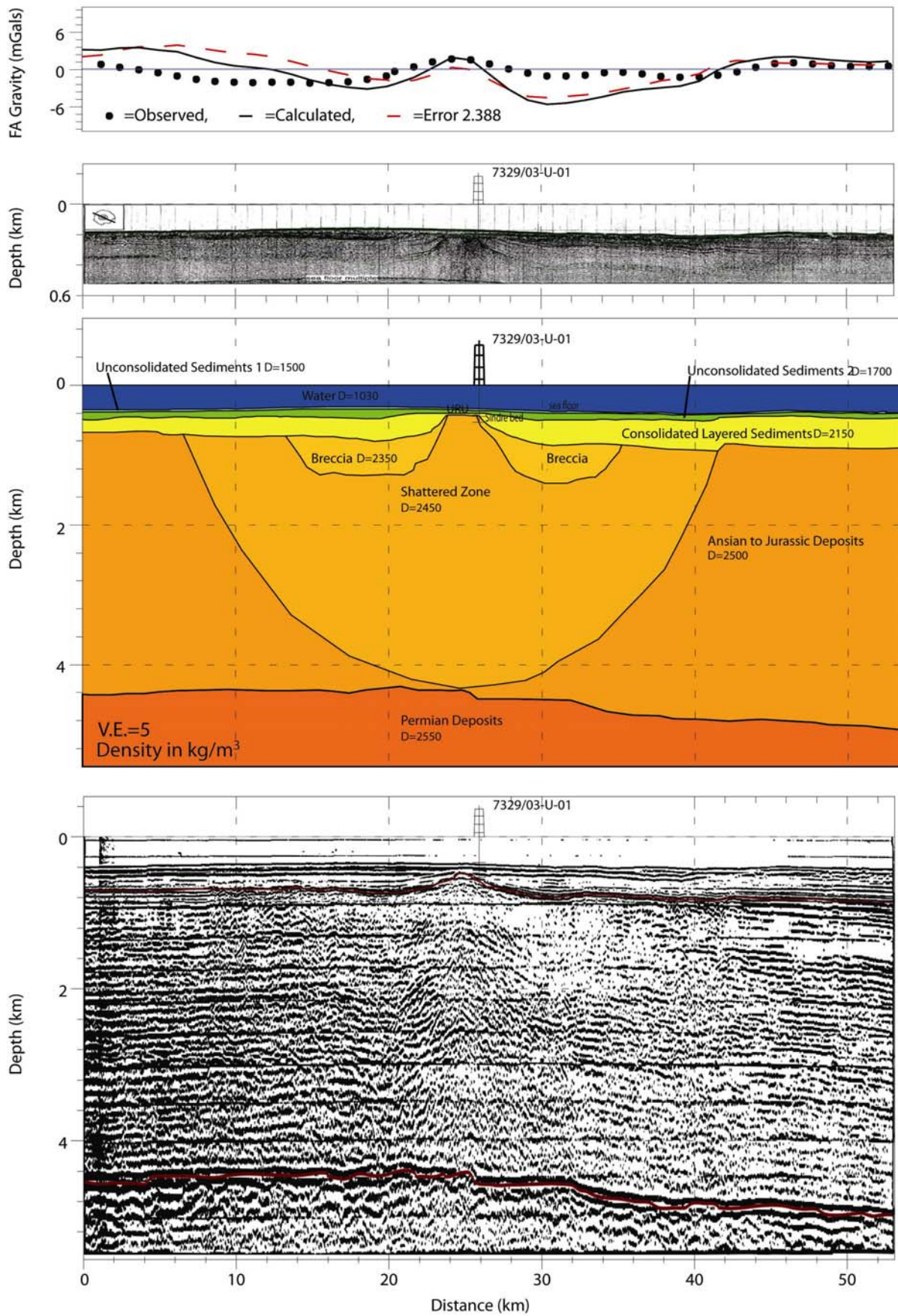


Fig. 8: The modelling results for a trend-corrected anomaly, both seismic images and the density model.

density due to shattering of the surroundings and (2) the uplift of deeper and denser layers in the centre. The former features a broad relative low and the latter adds a central relative high to the gravity anomaly. The model accounts for this and consists of eight model bodies: Unconsolidated Sediments 1, Unconsolidated Sediments 2, Consolidated Layered Sediments, Breccia, Shattered Zone, Ansian to Jurassic Deposits, and Permian Deposits. The characteristic densities and the unit description and boundary justifications are given in Tab.1.

Model body	Density [kg/m ³]	Body Characteristics Boundary (seismic horizon)
Water	1030	Seafloor
Unconsolidated Sediments 1	1500	Stratification Seismic reflector
Unconsolidated Sediments 2	1700	Stratification Late Cenozoic upper regional unconformity
Consolidated Layered Sediments	2150	Stratification Base Cretaceous (Reflector)
Allochthonous and Autochthonous Breccia	2400	Disturbed stratification (void)
Shattered Zone	2450	Disturbed stratification
Ansian to Jurassic Deposits	2500	Undisturbed stratification Top Permian (Reflector)

Table 1: Model bodies, model densities, body characteristics and boundary description.

The observed free air gravity anomalies and the calculated gravity anomalies are given in Fig. 8. Densities assigned to the uppermost model bodies are chosen similar to the densities measured for the core samples (Fig. 4), although increased compaction could very well have taken place at greater depth. The major uncertainties for this model are the densities of the uppermost layers representing unconsolidated sediments for which the first 70 m of the core were lost. Naturally, the uppermost layers influence the model response the most, especially if the density contrast is high, and do not leave much interpretational space for the deeper structure, here made up of bodies with very low density contrast. The first layers are unconsolidated Quaternary sediments, which may have densities less than 1700 kg/m³ and as low as 1300 kg/m³. In our model, horizons were picked from the high-resolution seismic profile, but the densities (1500 and 1700 kg/m³) could be overestimated, and thus result in shallower anomalies.

The dominant feature is the structural uplift of higher density material compared to the surrounding compacted or unconsolidated sedimentary layers. The upper boundary is well defined through the seismic profiles available, as opposed to the densities related to the layers. We observe that the amplitude of the observed gravity anomaly is somewhat smoother and shallower than the modelled values. One possible reason for this is that the modelling approach using a 2-dimensional cross-section, which in the case of a circular structure as craters results in an overestimation of the amplitude of relative lows and highs.

Assuming a symmetric distribution of the model bodies an asymmetric distribution of the calculated gravity anomaly is observed, when compared to the trend corrected observation. Therefore, we calculate the anomaly for the same model configuration, but with an additional layer, which represents the underlying bedrock and the top basement interface and compared to the uncorrected gravity signal (Fig. 9). The resulting modelled anomaly shows a better fit

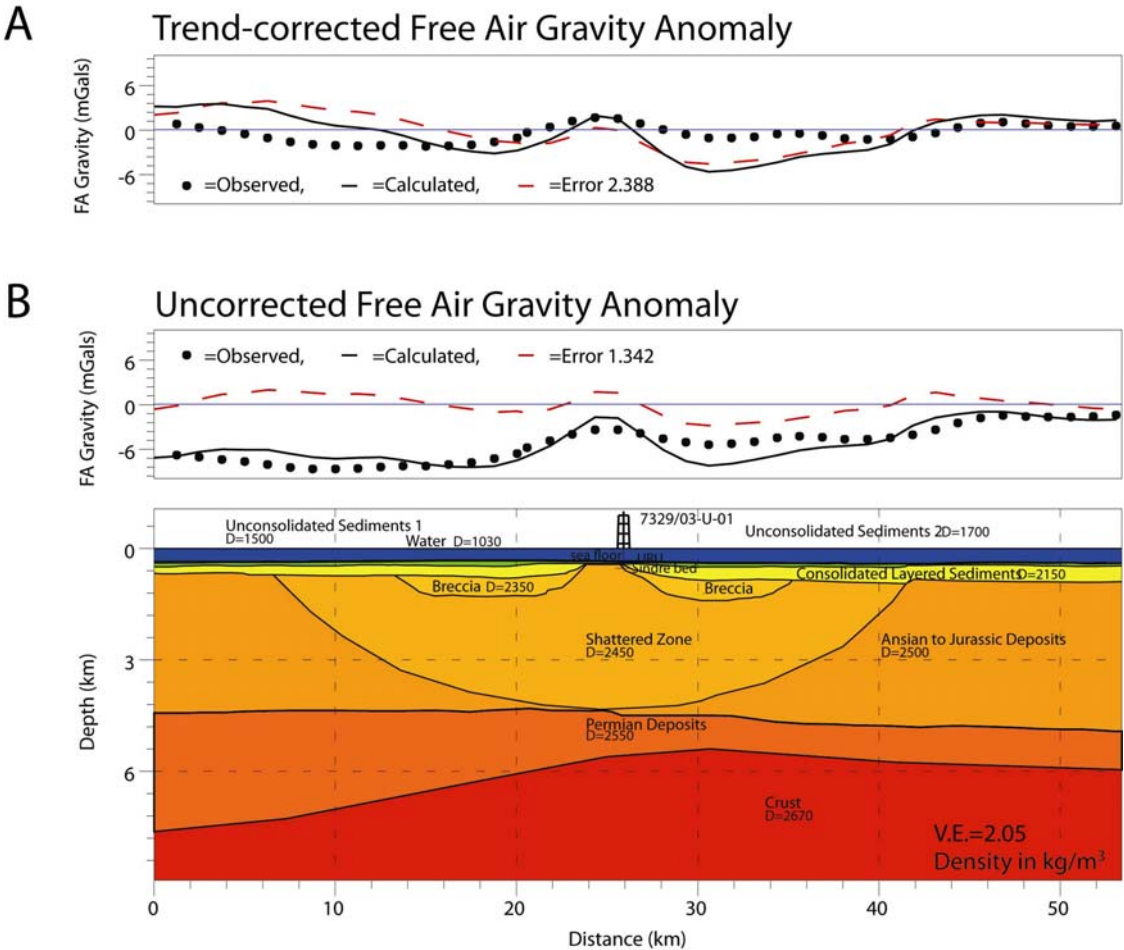


Fig. 9: A comparison between the modelling results for the trend corrected model as shown in Fig. 8 and the uncorrected one. The only difference is an additional interface (top basement), which separates the sedimentary body from bedrock. This interface is not constrained by seismics.

than for the corrected one, which is mainly due to the fact that the bedrock interface is not represented by a simple slope but more complex shape. For the trend correction, only a dipping layer was assumed when as simple slope was subtracted. From these models, the Mjølnir crater diameter itself is only about 20 km, and much smaller compared to earlier estimates (Tsikalas et al., 1998a,b,c). The area influenced by the impact event, due to shattering or disturbing the subsurface in the vicinity of the crater is larger. Also the intense and wide-ranging gravitational collapse as modelled by Shuvalov et al. (2002) might effect the morphology of that site, but cannot be resolved by gravity measurements.

6. CONCLUSIONS

Forward modelling suggests that the crater depth can be derived from joint interpretation of gravity and seismic data, and result in a reasonable interpretation. No clearly crater-related anomalies can be identified in the magnetic data, which suggests that the target material (sediments) does not show any properties that induce a magnetic signature, and that the projectile did not deliver any magnetizable material.

Details of the gravity anomaly could be related to the uppermost unconsolidated-sedimentary layers, as well as to deeper structures, both unrelated to the crater itself. Although we used a 2-dimensional modelling approach, which may result in an overestimation of the negative anomaly amplitude, the structural extent is reliable. We found that the actual crater diameter (rim-to-rim) is only about 20 km, which is similar in size to the Nördlinger Ries in southern Germany. Previous diameter estimates are based on the seismic interpretation of the shallow relief, and with the crater diameter being overestimated. We consider the dimensions derived from seismic data to cover the entire structure: Crater and ejecta blanket and related surge due to the water moving back to the impact site, and a result of differential compaction. A process also considered by Tsikalas et al. (2007).

We have also developed a detailed Cretaceous palaeogeographic reconstruction at the time of impact, and with relevance to tsunami modelling of the impact, the distance to Greenland was approximately the same as to Northern Norway (Finnmark) where waves as high as 100 meters have been estimated. We also demonstrate that the apparent southward drift of the Barents Sea region during Mid-Late Jurassic before continued northward drift (incidentally coinciding with the Mjølnir impact event) correlates with repeated coal occurrence in the East

Barents stratigraphy. These back-and-forth N-S movements and climatic change does not relate to 'continental drift' but are caused by true polar wander (TPW) during Jurassic and Early Cretaceous time. Barents Sea appears to be a good observational point for climatic changes due to TPW.

7. ACKNOWLEDGEMENTS

The BAS-06 survey was sponsored by Chevron, EniNorge, Norwegian Petroleum Directorate, RWE-Dea Norge and StatoilHydro. We acknowledge the effort by L. Gernigon and J.O. Mogaard in collecting and processing the survey data.

8. REFERENCES

- Breivik, AJ, Gudlaugsson, ST and Faleide, JI (1995) Ottar Basin, SW Barents Sea: A major Upper Paleozoic rift basin containing large volumes of deeply buried salt, *Basin res.* 7, 299-312.
- Dypvik, H, Gudlaugsson, ST, Tsikalas, F, Attrep Jr, M, Ferrell Jr, DH, Krinsley, DH, Mørk, A, Faleide, JI, and Nagy, J (1996) Mjølnir structure: an impact crater in the Barents Sea, *geology*, 24, 779-782.
- Dypvik, H, Sandbakken, PT, Postma, G, Mørk, A (2004) Early post-impact sedimentation around the central high of the Mjølnir impact crater (Barents Sea, Late Jurassic) *Sedimentary Geology*, 168(3-4), 227-247.
- Gernigon, L., Marello, L., Mogaard, J.O., Werner, S.C., Skilbrei, J.R. (2007) Barents Sea Aeromagnetic Survey BAS-06 - Acquisition - processing report and preliminary interpretation. Geological Survey of Norway. NGU Report no. 2007.035 (confidential to 01.12.2008). 144p.
- Glimsdal, S, Pedersen, GK, Langtangen, HP, Shuvalov, V, Dypvik, H (2007) Tsunami generation and propagation from the Mjølnir asteroid impact. *Meteoritics & Planetary Science*, 42(9),1473-1493
- Gudlaugsson, ST (1993) Large impact crater in the Barents Sea, *Geology*, 21, 291-294.
- Hammer, S (1963) Deep Gravity Interpretation by Stripping, *Geophysics* 28(3) 369.
- Johansen, SE, Ostistiy, BK, Birkeland, Ø, Federovsky, YF, Martirosjan, VN, Christensen, OB, Cheredeev, SI, Ignatenko, EA, Margulis, LS (1993) Hydrocarbon potential in the Barents Sea region: play distribution and potential, In: *Arctic Geology and Petroleum Potential*, Elsevier, Amsterdam, 273-320.
- Mauring, E, Kihle, O (2006) Leveling aerogeophysical data using a moving differential median filter, *geophysics*, 71(1), L5.
- Melosh, HJ (1989) *Impact Cratering: A Geologic Process*, 245 pp. Oxford Univ. Press, New York.
- Pesonen LJ, Lehtinen, M, Deutsch, A, Elo, S, Lukkarinen, H (1996) New Geophysical and Petrographic Results of the Suvasvesi N Impact Structure, Finland, *Lunar and Planetary Science*, 27, 1021.
- Reid, AB, Allsop, JM, Granser, H, Millet, AJ, Somerton, IW (1990) Magnetic interpretation in three dimensions using Euler deconvolution, *Geophysics* 55, 80-91.

- Shuvalov, V, Dypvik, H, Tsikalas, F (2002) Numerical simulations of the Mjølnir marine impact crater, *JGR* 107(E7), 5047, doi: 10.1029/2001JE001698.
- Skilbrei, JR, Kihle, O., Olesen, O., Gellein, J, Sindre, A, Solheim, D, Nyland, B (2000) Gravity anomaly map of Norway and adjacent ocean areas, scale 1:3 Million: Geological Survey of Norway (NGU), Trondheim.
- Smelror, M, Kelly, RA, Dypvik, H, Mørk, A, Nagy, J, Tsikalas, F (2001) Mjølnir (Barents Sea) meteorite impact ejecta offers a Volgian Ryazanian boundary marker, *Newsletter on Stratigraphy*, 38, 129-140.
- Steinberger, B, Torsvik, TH (2008) Absolute plate motions and true polar wander in the absence of hotspot tracks, *Nature* 452, 620 – 623.
- Talwani, M, Lamar Worzel, J, Landisman, M (1959) Rapid Gravity Computations for Two-Dimensional Bodies with Application to the Mendocino Submarine Fracture Zone, *JGR* 64, 49.
- Torsvik, TH, Olesen, O (1988), *Petrophysics and Palaeomagnetism initial report of the Norwegian Geological Survey Laboratory*, NGU report no. 88.171.
- Tsikalas, F, Gudlaugsson, ST, Faleide, JI (1998a) Collapse, infilling, and postimpact deformation at the Mjølnir impact structure, Barents Sea, *Geol. Soc. Am. Bull.*, 110 537-552.
- Tsikalas, F, Gudlaugsson, ST, Eldholm, O, Faleide, JI (1998b) Integrated geophysical analysis supporting the impact origin of the Mjølnir structure, Barents Sea, *Tectonophysics*, 289, 257-280.
- Tsikalas, F, Gudlaugsson, ST, Faleide, JI (1998c) The anatomy of a buried complex impact structure: The Mjølnir Structure, Barents Sea, *JGR*, 103(B12) 30469-30483.
- Tsikalas, F, Gudlaugsson, ST, Faleide, JI, Eldholm, O (2002) The Mjølnir marine impact crater porosity anomaly, *Deep-Sea Research II*, 49, 1103-1120.
- Tsikalas, F, Faleide, JI (2007) Post-impact structural crater modification due to sediment loading: An overlooked process, *Meteoritics & Planetary Science*, 42(11), 2013-2019.

9. FIGURES

Figure 1: The location of Mjølnir impact site (73°48' N, 29°40'E) within the southwestern Barents Sea.

Figure 2: The palaeogeographic setting of the Mjølnir impact site reconstructed to the Lower Cretaceous, ca.142 Ma. The main differences with respect to the current setting are the palaeo-latitude of 56.4°N and the then young and narrow Atlantic Ocean. The estimated tsunami wave height (after Glimsdal et al., 2007) and sedimentary basin outlines are draped on the reconstruction.

Figure 3: The Barents Sea in space and time. Along with the stratigraphic column for the southwestern Barents Sea and the Western Barents Sea basins, the magnetic polarity, the latitudinal drift of the Mjølnir impact site is shown. The drift curve is derived from a global apparent polar wander path with (red curve) and without (blue curve) corrections for true polar wander (TPW). The TPW corrected curve shows a general northward movement of the Barents Sea realm (with respect to the mantle) but the flat Jurassic-Early Cretaceous section of the curve show that the apparent Mid-Late Jurassic southward movement (with respect to the spin-axis) is an artefact of TPW.

Figure 4: The stratigraphy of core 7329/03-U-01 (Mørk, pers. comm. 2006) and measurements of susceptibilities (left) and densities (right) of competent samples. The red curve indicates the density variations with depth as used for the upper most layers of the density model.

Figure 5: The aeromagnetic anomaly map as surveyed during the BAS06 campaign. (a) Aeromagnetic measurements were performed along flight lines shown in red. Ship recordings of gravity and seismics are shown as black track lines. (b) The aeromagnetic anomaly map in comparison with the anomaly map of Tsikalas et al. (1998b); (c) the same in comparison with the palaeo-relief of Mjølnir as interpreted from seismic data by Tsikalas et al. (1998a,b,c); (d) palaeo-relief and a 10-km Gaussian high-pass filtered magnetic anomaly and (e) 20-km Gaussian high-pass filtered magnetic anomaly map; (f) example of the results of an Euler deconvolution with a structural index of SI=1 and a tolerance of 7 % applied to the 20-km Gaussian high-pass filtered magnetic anomaly in comparison with the palaeo-relief.

Figure 6: Free air gravity anomaly map (Skilbrei et al., 2000) in comparison with the palaeo-relief of Mjølnir (right), derived from seismic data by Tsikalas et al. (1998a, b, c), and (left) the gravity anomaly map provided by Tsikalas et al. (1998b).

Figure 7: Free air gravity anomaly map (top) in comparison with the palaeo-relief including on of the gravity profile across the structure in NW –SE direction, which coincides with two seismic lines, used in the 2D gravity modelling, profile plot (bottom), derived linear trends, as well as the trend corrected version of the anomaly.

Figure 8: The modelling results for a trend-corrected anomaly, both seismic images and the density model.

Figure 9: A comparison between the modelling results for the trend corrected model as shown in Fig. 8 and the uncorrected one. The only difference is an additional interface (top basement), which separates the sedimentary body from bedrock. This interface is not constrained by seismics.

10. TABLES

Table 1: Model bodies, model densities, body characteristics and boundary description.

11. APPENDIX

11.1 Susceptibility and Density Measurements:

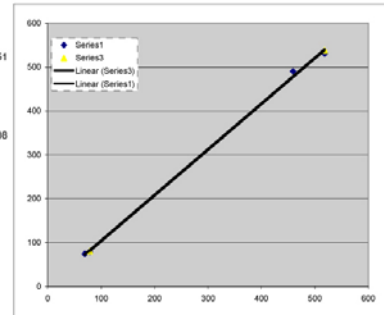
Susceptibilities were measured using a Bartington MS2c sensor in a core-scanning set-up, which only result in total susceptibilities. These measurements were calibrated by measuring a few test samples with the core scanner and in laboratorial condition.

Sample TL	VolumeTL	DensityTL	Suscept. TL	Sample SW	VolumeSW	Density SW	Suscept. SW	Sample SW	VolumeSW	Density SW	Suscept. SW								
3a	117.7399979	2469	49504.69922	Dry Samples				Wet Samples											
3b	117.6600037	2472	48839.30078																
3c	117.8199997	2469	48973.19922																
3d	117.6900024	2471	47511.69922																
3e	117.7799985	2469	49031.5																
	117.7380005	2470	48772.07969																
2a	118.1399994	2437	5835.259805									2ba	118.2699966	2412	5173.5	2aa	118.3700027	2436	5379.799805
2b	118.1200027	2438	5893.399902									2bb	118.2099991	2416	5347.200195	2ab	118.3399963	2437	5381.200195
2c	118.1200027	2438	5944.700195									2bc	118.1800003	2417	5485.399902	2ac	118.2200012	2438	5398
2d	118.0599985	2438	5848.700195									2bd	118.1100006	2418	5317.5	2ad	118.4100037	2436	5389.399902
2e	118.0599985	2438	5892.599902	2be	118.0899993	2419	5198.600098	2ae	118.4300003	2436	5354.259805								
	118.1160004	2437.8	5881		118.1719986	2416.4	5304.440039	530.444	118.3540009	2436.6	5380.539941	538.054							
1a	119.7600021	2420	885.5999756	1ba	119.7900009	2404	756.4000244	1aa	119.9800034	2424	788.7999878								
1b	119.7399979	2421	885.7000122	1bb	119.8199997	2406	789.9000244	1ab	119.8700027	2424	834.2999878								
1c	119.7900009	2420	874.0999756	1bc	119.7699986	2407	784.5999756	1ac	120.2099991	2419	781.7000122								
1d	119.7300034	2421	880.2000122	1bd	119.8700027	2406	800.7000122	1ad	120.0400009	2421	822								
1e	119.7099991	2421	885.9000244	1be	119.7799988	2408	823.7999878	1ae	119.9199982	2423	794.7999878								
	119.7460007	2420.6	882.3		119.8059998	2406.2	791.0800049	79.108	120.0040009	2422.2	804.3199951	80.432							
				2ka	94.23999786	2409	4857.799805												
				2kb	94.29000092	2410	5069.600098												
				2kc	94.29000092	2411	4855.299805												
				2kd	94.30999756	2411	5032.899902												
				2ke	94.33999634	2411	4909.899902												
					94.29399872	2410.4	4905.099902	490.51											
				1ka	92.54000092	2515	710.7999878												
				1kb	95.95999908	2428	748.4000244												
				1kc	95.88999939	2431	735												
				1kd	96	2430	755.0999756												
				1ke	96	2430	776.0999756												
					95.27799988	2440.8	745.0799927	74.508											

DORA Mess	Sample	Suscept: Dora
783.34	2b	518.2122254
693.83	2s	458.9976107
118.43	1b	78.34640623
104.82	1s	69.34282108

Dora-Measure	Dry-Lab	DORA	Wet_lab
78.41697069	79.10800049	78.41697069	80.43199951
518.2122254	530.4440039	518.2122254	538.0539941
69.28328231	74.50799927	69.28328231	74.50799927
458.9976107	490.50999902	458.9976107	490.50999902
		DORA	Wet_lab
		78.41697069	80.43199951
		518.2122254	538.0539941

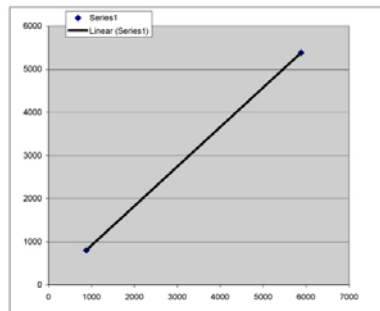
Dora_Wet_Corr	1.04053418
Dora_Dry_Corr	1.041729118



Correlation Wet_LAB TL vs. SV:

5881	5380.539941
882.3	804.3199951

0.915482019



The smaller sample set was measured in a laboratory environment (Torsvik and Olesen, 1988), and both volume-specific susceptibilities and densities were determined.

ID	Sample	Density Suscept		
		Volume cm ³	kg/m ³	10 ⁻⁶ SI
1	first	0	0	0
2	22	128.8200073	2383	448
3	1	85.04000092	2251	149.8999939
4	5	42.22999954	2252	413.2000122
5	18	42.61000061	2451	661.5999756
6	6	30.04999924	2928	1563.900024
7	15	26.07999992	2618	1029.5
8	12	31.07999992	1907	323.8999939
9	13a	58.52000046	2399	550.5
10	13b	17.92000008	2400	337
11	2	62.58000183	2329	150.1000061
12	8	49.54000092	2269	94.80000305
13	7	72.44000244	2412	268.6000061
14	14	53.09000015	2455	353.8999939
15	20	62.79999924	2406	577.0999756
16	9	57.88000107	2366	371
17	17	45	2405	268.3999939
18	10	15.67000008	1678	385.3999939
19	19	25.21999931	2379	345.8999939
20	16	24.60000038	2413	190.8999939
21	21	83.54000092	2390	281.2000122
23	24	79.06999969	2381	271.6000061
24	23	49.15000153	2354	273.1000061
25	11	9.430000305	1589	284.7000122
26	3	20.22999954	1961	597.2000122
27	4	13.69999981	2014	195.8999939